Nano Research
2020, 13(4): 947–951

ISSN 1998-0124 CN 11-5974/O4
https://doi.org/10.1007/s12274-020-2720-1

Research Article

Fabricating Pd isolated single atom sites on C_3N_4/rGO for heterogenization of homogeneous catalysis

Ninghua Fu[1], Xiao Liang[1], Zhi Li[1] (✉), Wenxing Chen[2], Yu Wang[3], Lirong Zheng[4], Qinghua Zhang[5], Chen Chen[1], Dingsheng Wang[1], Qing Peng[1], Lin Gu[5], and Yadong Li[1] (✉)

[1] *Department of Chemistry, Tsinghua University, Beijing 100084, China*
[2] *Beijing Key Laboratory of Construction Tailorable Advanced Functional Materials and Green Applications, School of Materials Science and Engineering, Beijing Institute of Technology, Beijing 100081, China*
[3] *Shanghai Synchrotron Radiation Facility, Shanghai Institute of Applied Physics, Chinese Academy of Sciences, Shanghai 201204, China*
[4] *Beijing Synchrotron Radiation Facility, Institute of High Energy Physics, Chinese Academy of Sciences, Beijing 100049, China*
[5] *Beijing National Laboratory for Condensed Matter Physics, Institute of Physics, Chinese Academy of Sciences, Beijing 100190, China*

Received: 15 September 2019 / **Revised:** 16 February 2020 / **Accepted:** 17 February 2020

ABSTRACT

Metal isolated single atomic sites catalysts have attracted intensive attention in recent years owing to their maximized atom utilization and unique structure. Despite the success of single atom catalyst synthesis, directly anchoring metal single atoms on three-dimensional (3D) macro support, which is promising to achieve the heterogenization of homogeneous catalysis, remains a challenge and a blank in this field. Herein, we successfully fabricate metal single atoms (Pd, Pt, Ru, Au) on porous carbon nitride/reduced graphene oxide (C_3N_4/rGO) foam as highly efficient catalysts with convenient recyclability. C_3N_4/rGO foam features two-dimensional microstructures with abundant N chelating sites for the stabilization of metal single atoms and vertically-aligned hierarchical mesostructure that benefits the mass diffusion. The obtained Pd_1/C_3N_4/rGO monolith catalyst exhibits much enhanced activity over its nanoparticle counterpart for Suzuki-Miyaura reaction. Moreover, the Pd_1/C_3N_4/rGO monolith catalyst can be readily assembled in a flow reactor to achieve the highly efficient continuous production of 4-nitro-1,1'-biphenyl through Suzuki-Miyaura coupling.

KEYWORDS

heterogenization of homogeneous catalysis, metal isolated single atoms, carbon nitride, reduced graphene oxide, monolith catalyst

1 Introduction

Homogeneous catalysts feature ultrahigh catalytic efficiency owing to the facile contact of reaction substrates with catalysts in the same phase [1]. Nevertheless, the difficulty of separating homogeneous catalysts from the products poses grand challenges in controlling the cost and purity of the product [2]. Nanocatalysts can be applied in both the liquid–solid phase and gas–solid phase reactions, which are readily separable from the reaction mixtures for another cycle of the catalytic reaction [3, 4]. However, metal utilization is low compared with homogeneous catalysts [5]. Metal isolated single atom sites (ISAS) catalysts have recently emerged as a family of heterogeneous catalysts that feature atomically dispersed, well-defined metal active sites resembling homogeneous catalysts [6–12]. To date, many ISAS catalysts have been reported with satisfactory catalytic properties, and most of these catalysts are solids that consist of a collection of large numbers of particles. For powder catalysts, their separation from the liquid/gas reaction phase and the ability for continuous production are inferior to the monolith catalyst, which defined as a single block of catalytic materials through which reactants and products are transported by convective processes (flow reaction) [13]. Anchoring isolated metal sites on a macroscopic solid support as the monolith catalyst represents an ideal strategy to achieve the heterogenization of homogeneous catalysts and to accelerate the reaction rate of nanocatalysts via exposing more active sites [14, 15]. Moreover, the application of the monolith catalyst facilitates the integration of single atom catalysts to macroscopic catalytic materials, so as to achieve continuous production of organic catalysis [16, 17]. Until now, although numerous methods have been developed for the synthesis of ISAS catalysts [18–23], little efforts have been devoted to fabricating atomic-level ISAS onto three-dimensional (3D) macroscale catalytic materials [24].

Two factors should be considered when designing the ISAS monolith catalysts. First, there should be abundant anchoring sites on the monolith support for the stabilization of metal single atoms [25]. Second, the support should be in the macroscopic dimension, which possesses an accessible internal surface for the efficient catalytic reaction [26, 27]. 3D reduced graphene oxide (rGO) foams are porous materials constructed by ultra-thin corrugated rGO nanosheets [28–30]. The rGO foams feature low density, high specific area, and tailorable shape, making it an ideal monolith support for ISAS active center. rGO foams can be assembled by hydrothermal treatment of two-dimensional

Address correspondence to Zhi Li, zhili@tsinghua.edu.cn; Yadong Li, ydli@tsinghua.edu.cn

(2D) graphene oxide (GO) nanosheets. The arrangement of 2D rGO sheets in 3D rGO foam can be rationally tuned by modifying the hydrothermal parameters [31]. rGO features anchoring sites for stabilization of metal single atoms, but the anchoring sites are sparse, making it difficult to prepare high-loading metal single atom catalysts. Combining rGO with 2D materials that possess abundant ligating atoms, such as carbon nitride (C_3N_4), is an effective strategy to tackle this challenge.

Herein, we report the rational design of M_1/C_3N_4/rGO (M = Pd, Pt, Ru, Au) monolith catalysts with 3D macrostructure for heterogenization of homogeneous catalysis. The porous and orderly assembled M_1/C_3N_4/rGO catalysts feature large specific area, well-defined channels for the facile mass diffusion and catalytic reaction between reactants and active sites. The Pd_1/C_3N_4/rGO catalytic foam exhibits much-improved activity than Pd nanoparticles for Suzuki-Miyaura reaction. When assembled in a flow reactor, the Pd_1/C_3N_4/rGO catalytic foam can realize the continuous production of 4-nitro-1,1'-biphenyl with steady reaction rates of about 12 mmol·g_{Pd}^{-1}·min^{-1}.

To fabricate 3D C_3N_4/rGO foam as the support, the 2D layered GO and C_3N_4 were separately synthesized as the starting materials (Fig. 1(a)). C_3N_4 was obtained by heating a mixture of dicyandiamide and ammonium chloride at a temperature of 550 °C. GO was prepared according to a modified Hummers' method, by which the natural graphite powder was chemically oxidized and exfoliated to single-layered structures (see the Electronic Supplementary Material (ESM) for detailed procedures). Scanning electron microscopy (SEM) image of GO showed an average lateral size of 10.14 μm (Fig. S1 in the ESM) and the Raman spectrum of GO displayed typical D- (1,340 cm^{-1}) and G-band (1,580 cm^{-1}) of GO with an I_D/I_G of 0.87 (Fig. S2 in the ESM). Thereafter, GO and C_3N_4 powders were suspended in a KOH aqueous solution and subjected to hydrothermal treatment. During this process, GO nanosheets partially converted to rGO and collaboratively assembled with C_3N_4 to form 3D macroscopic foams. The use of KOH during the hydrothermal treatment was the key to the formation of C_3N_4/rGO monolith with well-aligned microstructures. As can be seen from the SEM images (Figs. 1(b)–1(d)), the C_3N_4/rGO layers possessed orderly organized onion-like microstructure through the cross-section of C_3N_4/rGO foam cylinder. The C_3N_4/rGO walls were vertically aligned with an average distance of 25 μm and meanwhile linked with each other by some C_3N_4/rGO fragment. The orderly alignment and bridging of C_3N_4/rGO endowed the monolith with accessible internal surface and efficient mass transfer capability, which is essential to the catalytic property of M_1/C_3N_4/rGO monolith. C_3N_4/rGO monolith prepared under the same hydrothermal conditions without adding KOH led to disordered microstructures (Fig. S3 in the ESM). We measured the thickness of the GO sheets building block by the atomic force microscopy (AFM). The sheet height of about 0.7 nm corresponded to that of one individual GO layer (Fig. 1(e)).

The as-prepared C_3N_4/rGO foam was used as the support to adsorb Na_2PdCl_4 precursors and then calcined to decompose the metal precursor and anchor Pd single atoms onto C_3N_4/rGO (Fig. 1(a)). By analyzing the N_2 adsorption/desorption isotherms on Pd_1/C_3N_4/rGO, the Brunauer–Emmett–Teller (BET) specific surface area of Pd_1/C_3N_4/rGO catalytic foam was determined to be 132.9 $m^2 \cdot g^{-1}$ (Fig. S4 in the ESM). The morphology and

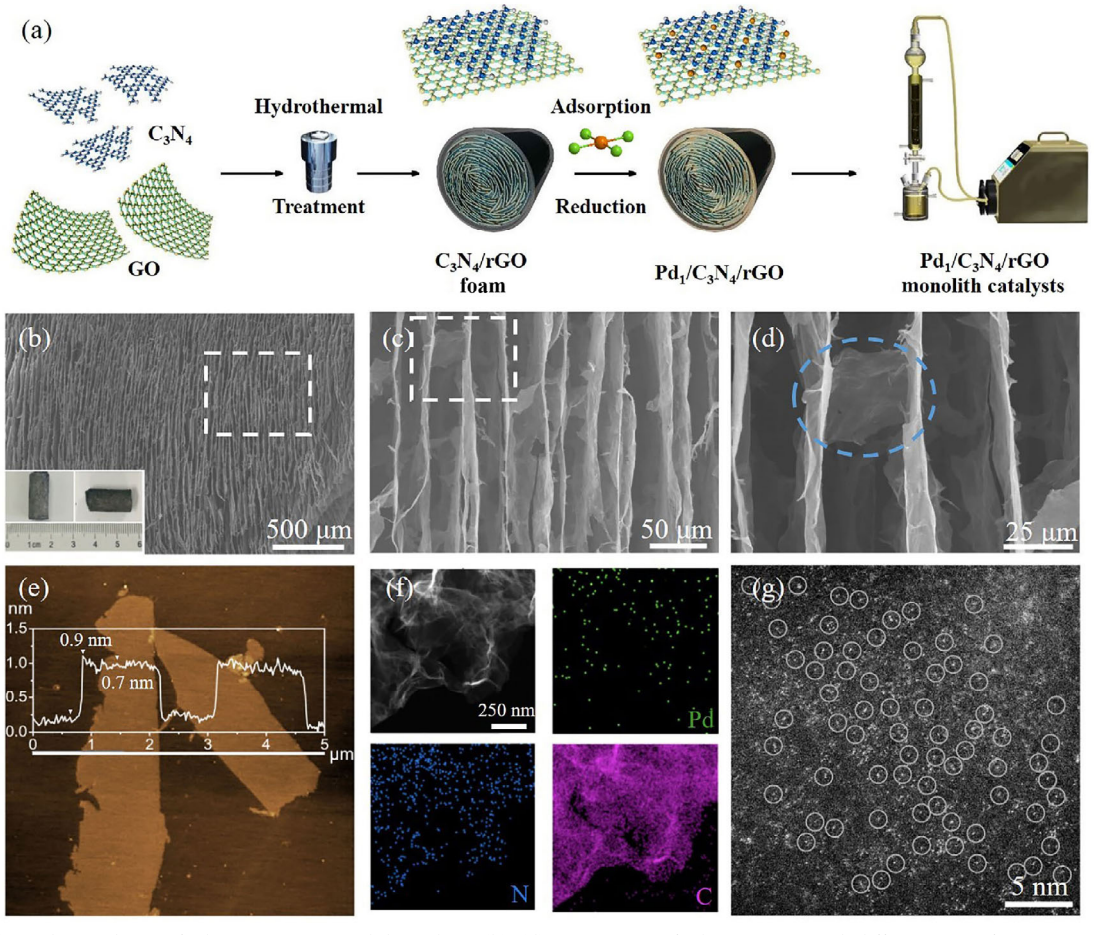

Figure 1 (a) Synthetic scheme of Pd_1/C_3N_4/rGO monolith catalysts. (b)–(d) SEM images of Pd_1/C_3N_4/rGO with different magnifications. Insets of (b) are the photographic images of the 3D Pd_1/C_3N_4/rGO monolith catalyst. (e) AFM image of GO substrate, (f) EDS elemental mapping and (g) high-resolution HAADF-STEM image of Pd_1/C_3N_4/rGO.

elemental distribution of Pd_1/C_3N_4/rGO were characterized by high-angle annular dark-field scanning transmission electron microscopy (HAADF-STEM) and energy-dispersive X-ray spectroscopy (EDS). As shown in the elemental mapping (Fig. 1(f)), the N and C constituted the main components of the hybrid layer with Pd elements homogeneously distributed on the substrate. In the HAADF-STEM image (Fig. 1(f)), no Pd nanoparticles were observed, indicating the Pd was ultra-finely dispersed in C_3N_4/rGO. Furthermore, we utilized high-resolution HAADF-STEM to observe the sample. It is clearly shown that the Pd existed as isolated single atom sites on the 2D C_3N_4/rGO sheet with no aggregated Pd nanoparticles or clusters (Fig. 1(g)), providing direct evidence for the existence of Pd single atoms.

Extended X-ray absorption fine structure (EXAFS) and X-ray absorption near-edge structure (XANES) measurements were performed to further characterize the atomic dispersion and electronic structure of Pd. The EXAFS curve of Pd_1/C_3N_4/rGO only showed one main peak located at about 1.5 Å, which could be attributed to the Pd–N(O) scattering path (Fig. 2(a)). On the contrary, the Pd–Pd peak at about 2.5 Å was not detected in the Pd_1/C_3N_4/rGO sample. The XANES curve of Pd_1/C_3N_4/rGO showed near-edge absorption energy between those of Pd foil and PdO (Fig. 2(b)), indicating the Pd atoms in the catalyst carried partial positive charges with an oxidation state between zero and bivalence. The oxidation stated of Pd_1/C_3N_4/rGO was also demonstrated by X-ray photoelectron spectroscopy (XPS) measurement. As shown in Fig. S6 in the ESM, the Pd 3d spectrum can be deconvoluted into two peaks at binding energies of 337.24 and 342.6 eV, corresponding to $3d_{5/2}$ and $3d_{3/2}$ level, respectively. The peak positions of Pd_1/C_3N_4/rGO are between those of Pd(II) and Pd(0).

These analyses demonstrated Pd atoms were atomically dispersed in the Pd_1/C_3N_4/rGO sample, consistent with the high-resolution HAADF-STEM observations. Wavelet transform (WT) of Pd K-edge EXAFS analysis, which features powerful resolutions in both k and R spaces, was carried out to further verify the atomic dispersion of Pd in Pd_1/C_3N_4/rGO (Fig. 2(c)). By comparing the WT contour plots of PdO and Pd foil, it can be discerned that the intensity maxima at about 5 and 8.0–8.5 $Å^{-1}$ were respectively correlated with Pd–O and Pd–Pd contributions. For the WT contour plots of the Pd_1/C_3N_4/rGO, only one intensity maximum at about 5 $Å^{-1}$ is detected, which could be attributed to the Pd–N(O) coordination, and no intensity maximum belonging to Pd–Pd contribution was observed. Furthermore, we performed EXAFS fitting to obtain the quantitative structural parameters of Pd in the Pd_1/C_3N_4/rGO. The EXAFS fitting parameters were listed in Table S2 in the ESM, and the fitting curves were exhibited in Fig. S5 in the ESM. Based on the EXAFS data and fitting results, we can infer the Pd was coordinated by three chelating nitrogen atoms on the C_3N_4 as shown in Fig. S5 in the ESM.

Based on the above analyses, we successfully fabricated the Pd_1/C_3N_4/rGO by a hydrothermal treatment of C_3N_4/rGO mixed suspension followed on the adsorption and reduction of Pd precursors. This method can be facilely applied for the preparation of other noble metal (Pt, Au, Ru) based ISAS/C_3N_4/rGO monolith catalysts. By replacing the Na_2PdCl_4 precursors with $Pt(acac)_2$, $Ru(acac)_3$ and $HAuCl_4$, Pt-ISAS, Ru-ISAS, and Au-ISAS on C_3N_4/rGO can be fabricated with similar experimental procedures (experimental details please refer to the ESM), respectively. Transmission electron microscopy (TEM) images (Figs. 3(a)–3(c)) and high-resolution HAADF-STEM images (Figs. 3(d)–3(f)) of Pt_1, Au_1, Ru_1/C_3N_4/rGO displayed two-dimensional microstructures with numerous bright metal single atoms distributed on the substrate. Loading content of each metal is seen in Tables S1 and S3 in the ESM.

Taking Pd_1/C_3N_4/rGO as a demonstration, we show how the M_1/C_3N_4/rGO monolith catalyst can be applied for enhanced catalytic efficiency. As is well known, Pd is one of the most powerful catalysts for carbon–carbon couplings, such as Suzuki reaction and Heck reaction. Herein, the Suzuki-Miyaura reaction was selected as a model reaction to study the catalytic behavior of Pd_1/C_3N_4/rGO. Pd_1/C_3N_4/rGO, as a monolith catalyst with pores and accessible catalytic sites, can be directly applied as catalysts for organic reactions in batch reaction. As shown in Fig. 4, for reaction in a flask with magnetic stirring, our Pd_1/C_3N_4/rGO exhibited much enhanced catalytic reactivity

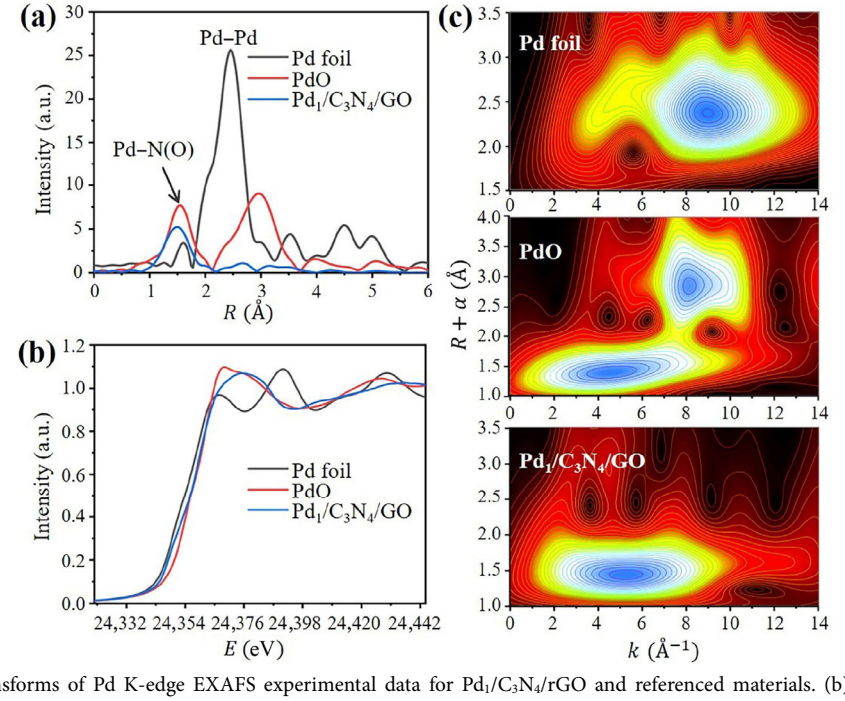

Figure 2 (a) Fourier transforms of Pd K-edge EXAFS experimental data for Pd_1/C_3N_4/rGO and referenced materials. (b) XANES of Pd K-edge for Pd_1/C_3N_4/rGO with reference materials Pd foil and PdO. (c) Wavelet transforms for the Pd K-edge EXAFS signals for Pd_1/C_3N_4/rGO and reference materials.

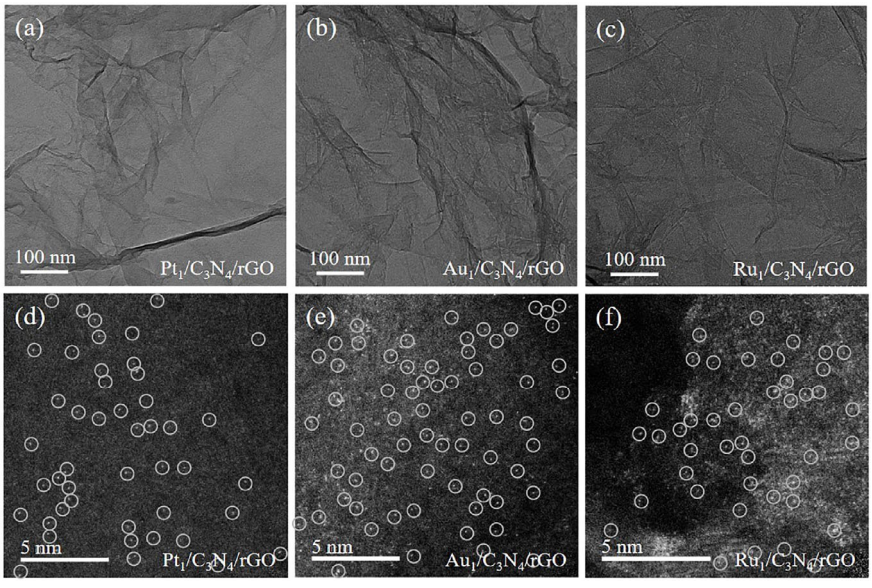

Figure 3 (a)–(c) TEM images and (d)–(f) high-resolution HAADF-STEM images of $Pt_1/C_3N_4/rGO$, $Au_1/C_3N_4/rGO$, $Ru_1/C_3N_4/rGO$ monolith catalysts, respectively.

than its nanoparticle counterpart $Pd_{nano}/C_3N_4/rGO$. The $Pd_1/C_3N_4/rGO$ was able to fully convert p-iodinitrobenzene into 4-nitro-1,1'-biphenyl in about 60 min (Fig. 4(a)). In contrast, the yield of $Pd_{nano}/C_3N_4/rGO$ was lower than that of $Pd_1/C_3N_4/rGO$ (Fig. 4(b)), indicating that downsizing Pd nanoparticles into Pd-ISAS on C_3N_4/rGO can improve the catalytic efficiency for Suzuki-Miyaura reaction.

On the other hand, the hierarchical structure, that is, the ordered arrangement of C_3N_4/rGO nanosheets, is also a vital factor for the catalytic performance of $Pd_1/C_3N_4/rGO$. The orderly assembly of C_3N_4/rGO nanosheets benefits the diffusion of reaction substrate within $Pd_1/C_3N_4/rGO$ monolith. In contrast, the disordered C_3N_4/rGO nanosheets units may bring in hindrance for the contact of organic substrate and Pd catalytic active sites. As shown in Fig. 4(a), and Figs. S7 and S8 in the ESM, the turnover frequency (TOF) value of $Pd_1/C_3N_4/rGO$ (362.37 h^{-1}) is significantly higher than that of Pd-ISAS on disordered C_3N_4/rGO foam (144.72 h^{-1}) and commercial Pd/C's TOF value (87.8 h^{-1}).

More importantly, in virtue of the 3D macrostructure of C_3N_4/rGO foam, $Pd_1/C_3N_4/rGO$ can be readily assembled in a flow reactor for continuous production. As shown in Fig. 4(c) and Fig. S9 in the ESM, the $Pd_1/C_3N_4/rGO$ monolith catalysts were placed in a home-made flow reactor. The reaction solution was added from the top of the glass column and recycled by a flow pump. The catalytic efficiency in a catalytic column (TOF value 374.43 h^{-1}) was very close to that stirred in a flask (TOF value 362.37 h^{-1}), suggesting the substrate diffusion was not compromised in the flow reactor. Comparing the Pd contents in $Pd_1/C_3N_4/rGO$ before and after flow reaction, it was concluded that almost no Pd atoms leached during the reaction (Table S1 in the ESM). Moreover, the elemental mappings and high-resolution HAADF-STEM of $Pd_1/C_3N_4/rGO$ after reaction in the flow reactor indicated the Pd elements retained as ISAS on the C_3N_4/rGO foam substrate (Figs. S10 and S11 in the ESM).

For the continuous production test, we pumped the liquid reaction mixture through the $Pd_1/C_3N_4/rGO$ monolith catalysts, collected and analyzed the product solution at the outlet of the catalytic column.

The $Pd_1/C_3N_4/rGO$ steadily catalyzed the Suzuki-Miyaura

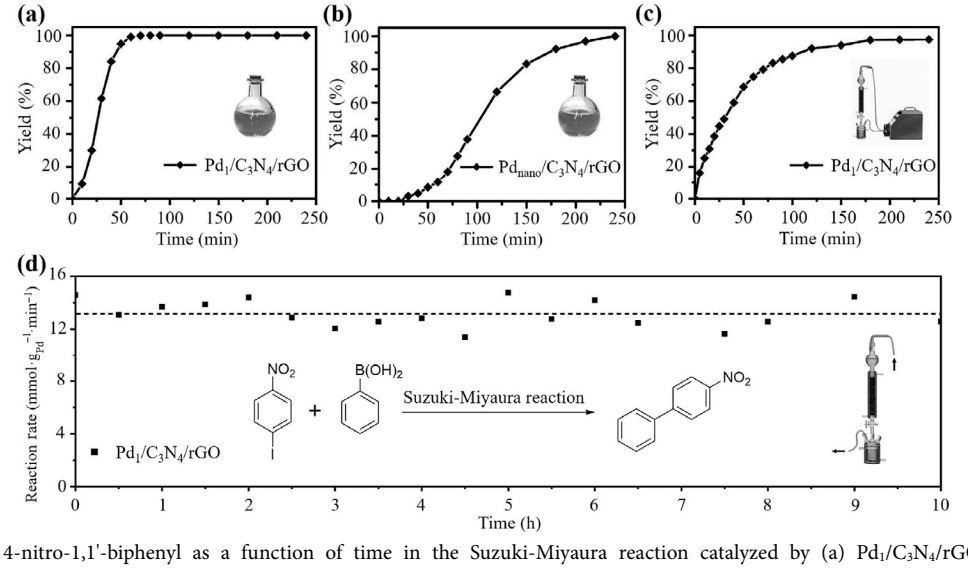

Figure 4 Yield of 4-nitro-1,1'-biphenyl as a function of time in the Suzuki-Miyaura reaction catalyzed by (a) $Pd_1/C_3N_4/rGO$ (batch reaction), (b) $Pd_{nano}C_3N_4/rGO$ (batch reaction), and (c) $Pd_1/C_3N_4/rGO$ (flow reactor). (d) The reaction rate (mmol·g_{Pd}^{-1}·min^{-1}) as a function of time-on-stream over $Pd_1/C_3N_4/rGO$ monolith catalysts in continuous-flow reactor.

reaction with production rates of 12.8 mmol·g_{Pd}^{-1}·min^{-1} during a 10-hour flow reaction test (Fig. 4(d)), demonstrating the versatile catalytic capability of Pd_1/C_3N_4/rGO monolith catalysts for both batch reactions and flow reactions.

In summary, we developed a general method for the fabrication of metal-ISAS on the 3D C_3N_4/rGO foams (Pd, Pt, Ru Au). The implementation of Pd_1/C_3N_4/rGO as novel single atom monolith catalysts allowed the efficient Suzuki-Miyaura reaction in both batch and flow reactions. The catalytic results also underlined the importance of an orderly-aligned assembly of C_3N_4/rGO nanosheets when designing 3D macro-ISAS catalysts. We believe this work will enlighten the manufacturing and application of single atom monolith catalysts for heterogenization of homogeneous catalysis with high-efficient continuous production.

Acknowledgements

This work was supported by the National Key R&D Program of China (No. 2018YFA0702003), the National Natural Science Foundation of China (No. 21890383 and 21971137) and Beijing Municipal Science & Technology Commission (No. Z191100007219003).

Electronic Supplementary Material: Supplementary material (SEM, HADDF-STEM and mapping imaging, and Raman spectroscopy measurements, etc.) is available in the online version of this article at https://doi.org/10.1007/s12274-020-2720-1.

References

[1] Bhaduri, S.; Mukesh, D. *Homogeneous Catalysis*: *Mechanisms and Industrial Applications*, 2nd ed.; Wiley: Hoboken, New Jersey, 2014.

[2] Shende, V. S.; Saptal, V. B.; Bhanage B. M. Recent advances utilized in the recycling of homogeneous catalysis. *Chem. Rec.* **2019**, *19*, 2022–2043.

[3] Wang, D. S.; Li, Y. D. Bimetallic nanocrystals: Liquid-phase synthesis and catalytic applications. *Adv. Mater.* **2011**, *23*, 1044–1060.

[4] Wu, Y. E.; Wang, D. S.; Li Y. D. Nanocrystals from solutions: Catalysts. *Chem. Soc. Rev.* **2014**, *43*, 2112–2124.

[5] Yang, X. F.; Wang, A. Q.; Qiao, B. T.; Li, J.; Liu, J. Y.; Zhang, T. Single-atom catalysts: A new frontier in heterogeneous catalysis. *Acc. Chem. Res.* **2013**, *46*, 1740–1748.

[6] Qiao, B. T.; Wang, A. Q.; Yang, X. F.; Allard, L. F.; Jiang, Z.; Cui, Y. T.; Liu, J. Y.; Li, J.; Zhang, T. Single-atom catalysis of CO oxidation using Pt_1/FeO_x. *Nat. Chem.* **2011**, *3*, 634–641.

[7] Kyriakou, G; Boucher, M. B.; Jewell, A. D.; Lewis, E. A.; Lawton, T. J.; Baber, A. E.; Tierney, H. L.; Flytzani-Stephanopoulos, M; Sykes, E. C. H. Isolated metal atom geometries as a strategy for selective heterogeneous hydrogenations. *Science* **2012**, *335*, 1209–1212.

[8] Yin, P. Q.; Yao, T.; Wu, Y. E.; Zheng, L. R.; Lin, Y.; Liu, W.; Ju, H. X.; Zhu, J. F.; Hong, X.; Deng, Z. X. et al. Single cobalt atoms with precise N-coordination as superior oxygen reduction reaction catalysts. *Angew. Chem., Int. Ed.* **2016**, *128*, 10800–10805.

[9] Chen, Y. J.; Ji, S. F.; Wang, Y. G.; Dong, J. C.; Chen, W. X.; Li, Z.; Shen, R. A.; Zheng, L. R.; Zhuang, Z. B.; Wang, D. S. et al. Isolated single iron atoms anchored on N-doped porous carbon as an efficient electrocatalyst for the oxygen reduction reaction. *Angew. Chem., Int. Ed.* **2017**, *129*, 7041–7045.

[10] Mitchell, S.; Vorobyeva, E.; Pérez-Ramírez, J. The multifaceted reactivity of single-atom heterogeneous catalysts. *Angew. Chem., Int. Ed.* **2018**, *57*, 15316–15329.

[11] Jones, J.; Xiong, H. F.; DeLaRiva, A. T.; Peterson, E. J.; Pham, H. Challa, S. R.; Qi, G.; Oh, S.; Wiebenga, M. H.; Hernández, X. I. P. et al. Thermally stable single-atom platinum-on-ceria catalysts via atom trapping. *Science* **2016**, *353*, 150–154.

[12] Wei, S. J.; Li, A.; Liu, J. C.; Li, Z.; Chen, W. X.; Gong, Y.; Zhang, Q. H.; Cheong, W. C.; Wang, Y.; Zheng, L. R. et al. Direct observation of noble metal nanoparticles transforming to thermally stable single atoms. *Nat. Nanotechnol.* **2018**, *13*, 856–861.

[13] Moulijn, J. A.; Kreutzer, M. T.; Nijhuis, T. A.; Kapteijn, F. Monolithic catalysts and reactors: High precision with low energy consumption. *Adv. Catal.* **2011**, *54*, 249–327.

[14] Chen, Z. P.; Vorobyeva, E.; Mitchell, S.; Fako, E.; Ortuño, M. A.; López, N.; Collins, S. M.; Midgley, P. A.; Richard, S.; Vilé, G. et al. A heterogeneous single-atom palladium catalyst surpassing homogeneous systems for Suzuki coupling. *Nat. Nanotechnol.* **2018**, *13*, 702–707.

[15] Zhao, C.; Yu, H. Z.; Wang, J.; Che, W.; Li, Z. J.; Yao, T.; Yan, W. S.; Chen, M.; Yang, J.; Wei, S. Q. et al. A single palladium site catalyst as a bridge for converting homogeneous to heterogeneous in dimerization of terminal aryl acetylenes. *Mater. Chem. Front.* **2018**, *2*, 1317–1322.

[16] Tang, Z. H.; Shen, S. L.; Zhuang, J.; Wang, X. Noble-metal-promoted three-dimensional macroassembly of single-layered graphene oxide. *Angew. Chem., Int. Ed.* **2010**, *122*, 4707–4711.

[17] Santana, J. S.; Skrabalak, S. E. Continuous flow routes toward designer metal nanocatalysts. *Adv. Energy Mater.*, in press, DOI: 10.1002/aenm.201902051.

[18] Liu, P. X.; Zhao, Y.; Qin, R. X.; Mo, S. G.; Chen, G. X.; Gu, L.; Chevrier, D. M.; Zhang, P.; Guo, Q.; Zang, D. D. et al. Photochemical route for synthesizing atomically dispersed palladium catalysts. *Science* **2016**, *352*, 797–800.

[19] Zhang, Z. L.; Zhu, Y. H.; Asakura, H.; Zhang, B.; Zhang, J. G.; Zhou, M. X.; Han, Y.; Tanaka, T.; Wang, A. Q.; Zhang, T. et al. Thermally stable single atom Pt/m-Al_2O_3 for selective hydrogenation and CO oxidation. *Nat. Commun.* **2017**, *8*, 16100.

[20] Li, Q. H.; Chen, W. X.; Xiao, H.; Gong, Y.; Li, Z.; Zheng, L. R.; Zheng, X. S.; Yan, W. S.; Cheong, W. C.; Shen, R. A. et al. Fe isolated single atoms on S, N codoped carbon by copolymer pyrolysis strategy for highly efficient oxygen reduction reaction. *Adv. Mater.* **2018**, *30*, 1800588.

[21] Wang, J.; Li, Z. J.; Wu, Y. E.; Li, Y. D. Fabrication of single-atom catalysts with precise structure and high metal loading. *Adv. Mater.* **2018**, *30*, 1801649.

[22] Qu, Y. T.; Li, Z. J.; Chen, W. X.; Lin, Y.; Yuan, T. W.; Yang, Z. K.; Zhao, C. M.; Wang, J.; Zhao, C.; Wang, X. et al. Direct transformation of bulk copper into copper single sites via emitting and trapping of atoms. *Nat. Catal.* **2018**, *1*, 781–786.

[23] Cao, L. N.; Liu, W.; Luo, Q. Q.; Yin, R. T.; Wang, B.; Weissenrieder, J.; Soldemo, M.; Yan, H.; Lin, Y.; Sun, Z. H. et al. Atomically dispersed iron hydroxide anchored on Pt for preferential oxidation of CO in H_2. *Nature* **2019**, *565*, 631–635.

[24] Wang, Y.; Mao, J.; Meng, X. G.; Yu, L.; Deng, D. H.; Bao, X. H. Catalysis with two-dimensional materials confining single atoms: Concept, design, and applications. *Chem. Rev.* **2019**, *119*, 1806–1854.

[25] Wang, A. Q.; Li, J.; Zhang, T. Heterogeneous single-atom catalysis. *Nat. Rev. Chem.* **2018**, *2*, 65–81.

[26] Roy, S.; Bauer, T.; Al-Dahhan, M.; Lehner, P.; Turek, T. Monoliths as multiphase reactors: A review. *AIChE J.* **2004**, *50*, 2918–2938.

[27] Du, R.; Zhao, Q. C.; Zhang, N.; Zhang, J. Macroscopic carbon nanotube-based 3D monoliths. *Small* **2015**, *11*, 3263–3289.

[28] Niu, Z. Q.; Chen, J.; Hng, H. H.; Ma, J.; Chen, X. D. A leavening strategy to prepare reduced graphene oxide foams. *Adv. Mater.* **2012**, *24*, 4144–4150.

[29] Hu, G. J.; Xu, C.; Sun, Z. H.; Wang, S. G.; Cheng, H. M.; Li, F.; Ren, W. C. 3D graphene-foam-reduced-graphene-oxide hybrid nested hierarchical networks for high-performance Li–S Batteries. *Adv. Mater.* **2016**, *28*, 1603–1609.

[30] Li, C. W.; Qiu, L.; Zhang, B. Q.; Li, D.; Liu, C. Y. Robust vacuum-/air-dried graphene aerogels and fast recoverable shape-memory hybrid foams. *Adv. Mater.* **2016**, *28*, 1510–1516.

[31] Yao, B. W.; Chen, J.; Huang, L.; Zhou, Q. Q.; Shi, G. Q. Base-induced liquid crystals of graphene oxide for preparing elastic graphene foams with long-range ordered microstructures. *Adv. Mater.* **2016**, *28*, 1623–1629.